Journal of Materials Chemistry A

Accepted Manuscript

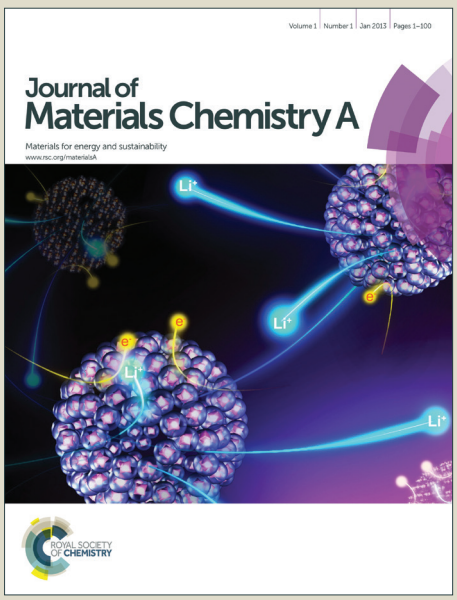

ROYAL SOCIETY OF CHEMISTRY

www.rsc.org/materialsA

Journal of Materials Chemistry A

Paper

Unusual Li-ion Storage through Anionic Redox Processes of Bacteria-driven Tellurium Nanorods

Received 00th January 20xx,
Accepted 00th January 20xx

DOI: 10.1039/x0xx00000x

www.rsc.org/

Min Gyu Kim,[a†*] Dong-Hun Kim,[c†] Taeyang Kim,[b] Sunhwa Park,[b] Gukyoung Kwon,[b] Mi Sug Kim,[a] Tae Joo Shin,[a] Hyungju Ahn[a] and Hor-Gil Hur[b*]

The bacterial respiration process enables the facile and morphologically-selective preparation of nanomaterials, along with the removal of environmentally toxic element. Bacteria-driven metallic tellurium Te(0) nanorods formed extra- and intracellularly through *Shewanella oneidensis* MR-1, consisting of the helically-twisted atomic-wire bundle structure, exhibited distinct Li-ion uptake properties after direct or glucose-assisted surface-carbonization of bacterial cells. By synchrotron-based *in situ* structural characterization during cycling, it was demonstrated that the carbonized polycrystalline Te materials experience phase transition to Li_2Te through simple Li-ion diffusion and charge compensation by the anionic redox reaction of metallic Te to polyanionic telluride (Te_n^{2-}). On the other hand, the carbonized amorphous Te materials show simple Li-ion accumulation around Te element with only the anionic redox reaction. The gradual generation of electrostatic interactions between Li^+ and Te_n^{2-} ion pairs promotes host lattice stabilization, unlike in other metallic anode systems with volume expansion. We report that the unusual anionic redox chemistry of Te with its structural flexibility drives the reversible Li-ion uptake without any critical structural deterioration, highlighting the potential of tellurium as a new energy conversion and storage material

Introduction

The metal-microbe interactions that occur during anaerobic bacterial respiration are important processes for the geochemical cycling of elements in soils, aquatic sediments, and subsurface environments. It is well-known that dissimilatory metal reducing bacterium *Shewanella* species play an important role in the global cycle of iron, manganese and trace metals, and are useful for many biotechnological applications such as bioremediation of waters and sediments contaminated with organics, metals, and radionuclides. The alternation of metal oxidation states by bacterial respiratory reduction activities has been applied to remediate environments contaminated with toxic heavy metals and metalloids. Moreover, the anaerobic respiration processes of *Shewanella* strains have recently been exploited as facile synthetic strategies toward nanostructured metal oxide and chalcogenide materials, with morphological control under ambient conditions in the absence of further chemical or thermal treatments.[1-7]

Over the last few decades, tellurium has been extensively used as an important atomic component in diverse application fields of photovoltaic solar panels,[8-10] piezoelectric,[11] thermoelectric devices[12,13] as well as phase-change memory devices,[14-16] despite its rarity in the Earth's crust.[17] These recent applications have led to a critical increase of highly toxic soluble oxyanions such as tetravalent tellurite and hexavalent tellurate known to be harmful to human cells.[18] Here, the anaerobic bacterial respiration process has been considered as a potential strategy for mitigating the environmental contamination through reduction to metallic Te(0) with low bioavailability and toxicity.[19,20] Along with the biological reductions of metal species such as Fe(III), U(VI) and Se(IV), *S. oneidensis* MR-1 has shown to reduce Te(IV) to metallic Te(0) *via* its respiratory system as a final electron acceptor under anaerobic conditions, simultaneously forming Te nanorods as a valuable side-benefit and controlling their morphologies.[21] This transformation could support a new and effective synthetic strategy for the morphologically-selective preparation of metallic Te nanomaterials.

A number of chemical and physical synthetic approaches toward nanostructured Te have been reported, including the uses of hydrothermal, vapor deposition, microwave-assisted, photon-induced and photolytic methods as well as surfactants.[22-27] Also, the morphologies have been extensively controlled to prepare wire-, tube-, rod-, tripod- and hexapod-type nanostructures, which can then be grown into hierarchical microstructures.[28-33] Interestingly, the metallic Te nanomaterials have an integrated geometry of close-packed atomic wires. Their crystal structures are composed of intrachains as atomic wires by the helical ordering of two-fold tellurium atoms, and interchains by close-packing of the individual intrachains (Fig. 1a). The van der Waals interactions between interchains form an empty volume space.[34] Here, we considered a

[a] Pohang Accelerator Laboratory (PAL), Pohang 790-784, Republic of Korea. E-mail: mgkim@postech.ac.kr
[b] School of Environmental Science and Engineering, Gwangju Institute of Science and Technology (GIST), Gwangju 500-712, Republic of Korea. E-mail: hghur@gist.ac.kr
[c] Geologic Environment Division, Korea Institute of Geoscience and Mineral Resources, Daejeon 305-350, Republic of Korea. E-mail: donghun80@gmail.com
† These authors contributed equally to this work.
Electronic Supplementary Information (ESI) available: See DOI: xx.xxxx/xxxxxxxxxx

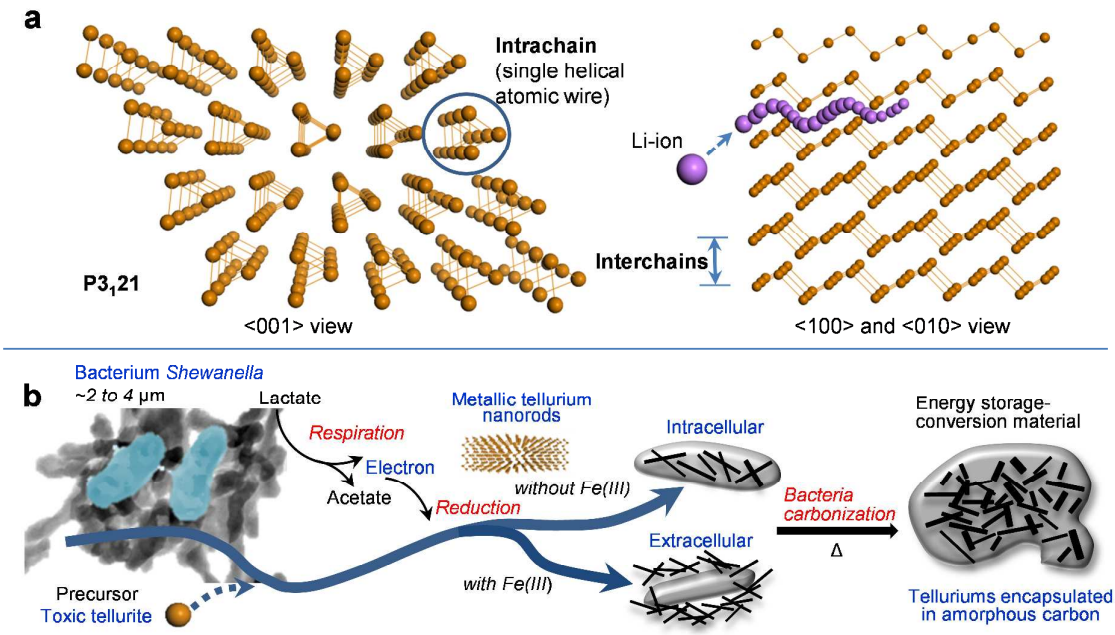

Fig. 1. Syntheses, morphologies and structural characterizations of Te nanorods. (**a**) Crystal structure of metallic Te under space group of $P3_121$, consisting of helically-twisted atomic wire (intrachain) and their close-packing (interchain). (b) *S. oneidensis* MR-1 metabolized lactate during respiration, reducing tellurite (TeO_3^{2-}) to Te(0). Depending on the presence of Fe(III), extracellular and intracellular Te(0) nanorods were selectively formed. The Te nanorods can be surface-modified during the direct and glucose-assisted carbonizations of organic bacterial cells.

Te nanorod as a bundle of helically-twisted atomic wires in which an external atomic element or ionic species can travel freely. In this study, these intrinsic structural characteristics could motivate the biogenic Te nanorods to create newly an application field for intercalation chemistry.

Given its ability to intercalate external ions, a potential application of Te can be envisioned in the arena of Li-ion rechargeable battery systems, where Li-ions could be reversibly taken up and released into and from the host lattice during discharge and charge processes, respectively. Recently, previous first report for the Te electrode material has been found in the Te/C composite through thermal-induced impregnation of liquid (melted) Te into porous carbon, showing the reversible volumetric charge capacity of 1400 mA h cm^{-3} (~224 mA h g^{-1}, corresponding to ~1.0 mole Li-ion release) in cathodic voltage profile between 2.5 and 1.0 V.[35] Another cathodic electrochemical behavior can be also observed in the Te-incorporated ordered mesoporous carbon composite, in comparison with volumetric capacities of sulphur and selenium electrodes.[36] Many intensive studies have tried to identify candidate energy conversion-storage materials, focusing on how much, how constant, how fast, and how long Li-ions can be intercalated and de-intercalated into/from host lattices without any structural deterioration during electrochemical cycling. Among them, nanostructured energy storage materials with fine-tuned morphologies and surface-coating appear to be the best candidates for meeting the Li-ion storage ability and fast conduction requirements. Generally, it is well-known that carbon coating onto single metallic nanostructured anode materials promotes an electrical contact between nanoparticles and minimizes both large volume change and side reaction in solid-electrolyte interface region during lithiation/delithiation processes.

Here, in order to meet the prerequisites such as one-dimensional morphology with high aspect ratios and surface carbonization of the nanomaterials, the present *S. oneidensis* MR-1 bacterial respiration process, tuned by the culture conditions, is designed primarily to prepare morphologically well-controlled Te nanorods, and secondarily, to allow direct carbonization of the organic bacterial cells around the nanorods, as schematically illustrated in Fig. 1b. Similar biological synthetic approaches using virus as a morphological template have been introduced to obtain effective nanostructured Li-ion electrode materials through simple adsorption of precursor or active element on the surface of virus.[37,38] Both uniformed shape and self-assemble characteristics of virus directly drove the preparation of well-designed nanostructured electrode materials. However, the virus was only used as a morphological-supporting material and did not contribute on the direct biological formation of active materials through biological reaction. In this research, on the other hand, *S. oneidensis* MR-1 offers a bi-functionality of facile biogenic preparation for metallic Te nanorods during bacterial respiration process and direct supply of carbon source after thermal carbonization. The electrochemically-inactive bacteria are overall distributed in the as-prepared Te nanorod matrix after bacterial respiration, which can be a drawback for usage of electrode material. Especially, the as-prepared intracellular Te has been encapsulated within bacterial cell. Therefore, simple burning process for the organic bacteria was inevitable. The thermal removing of bacterial cell can be helpful to

provide Te nanophases with additional electrical conductive carbon in the facile biological synthesis.

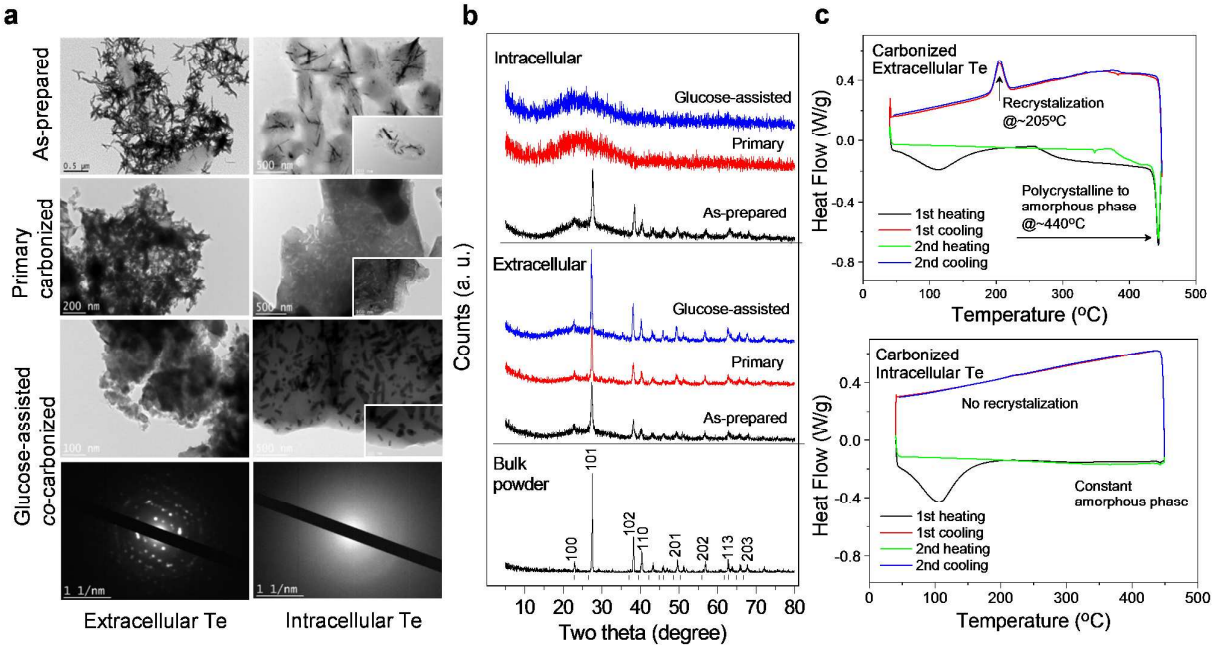

Fig. 2. Morphologies, structure and thermal analysis. (**a**) TEM images for as-prepared, primary carbonized and glucose-assisted *co*-carbonized Te materials with small area electron diffraction (SAED) patterns. Additional TEM and SEM images are available in Figs. S1-S3, ESI. (**b**) Corresponding XRD patterns. (**c**) Differential scanning calorimetric (DSC) analysis of carbonized extra- and intracellular Te. DSC measurements were performed in N_2 flow on heating to 450 °C at a rate of 10 °C/min using a DSC Q20 of TA Instruments.

Results and discussion

Structural and morphological changes of bacteria-driven Te nanorods during thermal removal of *S. oneidensis* MR-1

The Te nanorods were prepared under two different anaerobic respiration conditions for *S. oneidensis* MR-1. First, strain MR-1 produced uniform metallic Te nanorods extracellularly in the presence of Fe(III), in which both tellurite and Fe(III) function as electron acceptors in the anaerobic respiration process. TEM images show that the as-prepared extracellular Te nanorods are ~240 nm in length and 25 nm in width (Fig. 2a and Fig. S1, ESI).[21] Another bacterial synthetic pathway in the absence of Fe(III) provided intracellular Te nanorods with lengths of 100–200 nm and widths of ~10 nm.[5] The intracellular Te rods are anticipated to attain better electrical contact through the direct carbonization of the organic bacterial cells (Fig. S2, ESI). All X-ray diffraction (XRD) peaks of the as-prepared extra- and intracellular Te nanorods can be assigned to the typical trigonal phase of a = 4.45 Å and c = 5.92 Å under space group $P3_121$ (Fig. 2b). To eliminate the bacterial cells from the Te nanorod matrix, the as-prepared Te nanorods were carbonized under N_2 atmosphere at 600 °C, without or with glucose as an additional carbon source. After the primary carbonization, the initial free-standing extracellular Te nanorods were aggregated, while roughly retaining the nanorod structure. Thermal glucose-assisted *co*-carbonization showed clear particle agglomeration with the disappearance of the nanorod shape (Fig. 2a and Fig. S1, ESI). In contrast, both primary and glucose-assisted *co*-carbonized intracellular Te substrates presented constant rod-shape within the carbon matrix generated after burning the organic bacterial cells (Fig. S3, ESI). The EDX analysis for the as-prepared extra- and intracellular Te before and after carbonization present that the weight ratio of carbon to tellurium change from initial high values of values of 46 and 40 to 2 and 8 weight %, respectively. The carbon amounts in the carbonized biogenic Te are relatively little, compared to ~50% of Te/Carbon composite and ~30% of Tellurium@Ordered Macroporous Carbon Composite through chemical synthetic method (Fig. S4, ESI).[35-36] XRD and selected area electron diffraction (SAED) patterns reveal that the intracellular Te nanorods were unexpectedly changed to an amorphous phase upon carbonizations, whereas the extracellular Te nanorods retained the polycrystallinity (Fig. 2a and 2b).

The origin for the thermal evolution of different phases can be inferred with thermal behavior of bacterial organic carbon. The difference between intra- and extracellular Te is simply existence region of the Te nanorods inside and outside bacterial cell, respectively. Before heating, two as-prepared telluriums have commonly polycrystalline phase. As shown in thermal analyses (Fig. 2c, Figs. S4 and S5, ESI), on heating closed to 450 °C, differential scanning calorimetric curves present that two telluriums commonly experience in turn the dehydration and molecular relaxation, thermal decomposition of bacterial organic elements, and the phase transition to amorphous phase. During being cooled, however, the intracellular Te keeps constantly the amorphous phase, while the extracellular Te recovers the polycrystalline phase. It is clear that the Te encapsulated inside bacteria can be thermally affected by the amorphous carbon formed by thermal decomposition of organic bacteria, while the Te outside bacteria is

relatively free to the bacterial thermal decomposition. Therefore, it is possible that the carbon closed to melted Te can be partially thermal-diffused into the amorphous Te phase and then the diffused carbon prevents the melted Te from being reversibly assembled and recrystallized during cooling process. As a result, it can be reasonable that the carbon from the bacteria gives rise to a short-range ordered phase in the intracellular Te, unlike in the case of extracellular Te.

Li-ion uptake abilities after bacterial cell burning

The first discharge-charge voltage profiles of extra- and intracellular Te nanorods were obtained for as-prepared, primary and glucose-assisted *co*-carbonizations with current density of 80 mA g^{-1}, respectively (Fig. 3 and Figs. S6-S10, ESI). For the glucose-assisted *co*-carbonized Te substrates, different voltage profile characteristics were observed for the two nanorod morphologies: the amorphous intracellular Te substrate presented a smooth single profile, and the crystallized extracellular Te substrate showed two distinct plateaus at 1.6 and 0.8 V, suggesting different Li-ion uptake mechanisms. The as-prepared extracellular Te nanorods exhibited intrinsically low capacity because the polycrystalline nanophases seem to be mixed with the organic bacterial cells (Fig. 3a and Fig. S7, ESI). After primary carbonization, the first discharge and charge capacities dramatically increased to 780 and 510 mA h g^{-1}, respectively, because the insulating organic bacterial cells appear to be converted to an amorphous conductive carbon phase. As early as the 5th cycle, however, the charge capacity began gradually to fade to 355 mA h g^{-1}, which is close to the theoretical capacity (372 mA h g^{-1}) of commercial graphite LiC_6. The carbonized extracellular Te nanorods showed charge capacity retention of ~70% until the 50th cycle (Fig. 3c). Such capacity fading in nanostructured electrode materials is generally due to the severe loss of electrical contact between the free-standing nanomaterials during the Li-ion charge-discharge process.[39]

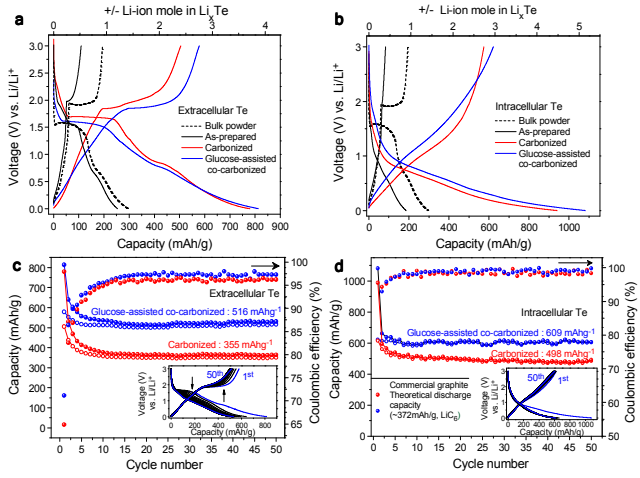

Fig. 3. Voltage profiles and cycle properties of Te nanorods. First discharge-charge voltage profiles of as-prepared, primary carbonized, and glucose-assisted *co*-carbonized (**a**) extracellular and (**b**) intracellular Te at a current density of 80 mA g^{-1}, compared to bulk Te powder. The Li-ion mole ratios were estimated from the capacities, based on a capacity of ~210 mA h g^{-1} for 1 mol Li-ion uptake per 1 mol Te (Te ↔ LiTe). Discharge (filled circles) and charge (open circles) capacities of glucose-assisted *co*-carbonized (**c**) extracellular and (**d**) intracellular Te over 50 cycles at a current density of 80 mA g^{-1}. Each inset presents 50 cycle voltage profiles.

After glucose-assisted *co*-carbonization of the extracellular Te nanorods, the first discharge and charge capacities were slightly improved to 820 and 580 mA h g^{-1}, respectively. On the other hand, the charge capacity retention increased to 90% in the 50th cycle. The initial discharge and charge capacities corresponded to the chemical compositions of $Li_{3.8}Te$ and $Li_{2.8}Te$, respectively, since the theoretical capacity of Te corresponds to 210 mA h g^{-1} per mol Li-ion uptake. This means that 3.8 mol Li^+ is inserted into the helical Te lattice in the fully discharged state, and a net 2.8 mol Li^+ is reversibly released in the subsequent charging process. After the first cycle, about 1.0 mol Li^+ cannot be reversibly extracted from the lithiated Te lattice, reflecting the initial low Coulombic efficiency of ~72%. After the 5th cycle, the Coulombic efficiency was greatly improved (>95%), and the charge capacities remained constant with 516 mA h g^{-1} even over the 50th cycle. The small charge capacity loss was probably associated with the gradual disappearance of the charge voltage plateau at 1.8 V (inset of Fig. 3c and Fig. S8, ESI). With a closer look at the 50th cycle profile, the corresponding discharge capacity clearly decreased at the 1.6 V plateau as a counterpart region and the overall profile evolved to a smooth single line after the 5th cycle, revealing the extinction of a certain Li-ion uptake mechanism for this voltage plateau. The electrochemical characteristics in this voltage region is comparable to recent result for Te-C composite with the reversible charge capacity of 224 mA h g^{-1} (corresponding to ~1 mol Li-ion release and volumetric capacity of 1400 mA h cm^{-3} in current density of 50 mA g^{-1}).[35] As a result, it is clear that ~2.5 mol Li^+ can be reversibly discharged and charged in the *co*-carbonized extracellular polycrystalline Te nanorods.

Secondly, the as-prepared intracellular Te nanorods embedded in the bacterial cells also showed very low Li-ion uptake near 100 mA h g^{-1} (Fig. 3b and Fig. S7, ESI). On carbonization of the bacterial cells unexpectedly led to the amorphous phase, the voltage profile was clearly changed to a single broad line without any distinct plateau and a lower voltage feature, which may be more suitable as an anode material. Compared to the carbonized extracellular polycrystalline nanomaterial, the first discharge and charge capacities of the carbonized intracellular amorphous Te were greatly enhanced to 990 and 618 mA h g^{-1}, respectively (Fig. 3d). The average charge capacity until the 50th cycle was nearly 500 mA h g^{-1} with 2.4 mol Li-ion uptake. The much higher initial capacity of the biogenic intracellular Te seems to result primarily from a morphological benefit with more efficient electrical contact by encapsulation in the carbon matrix from the *in situ* thermal burning of the bacterial cells. The burned bacteria can be considered to be carbon containers for the electrochemically active Te phases. As in the extracellular case, glucose-assisted *co*-carbonization of the intracellular Te nanorods promoted much increases to 1085 and 620 mA h g^{-1} in the first discharge and charge capacities, corresponding to chemical compositions of about $Li_{5.2}Te$ and $Li_{3.0}Te$, respectively. For the first cycle, irreversibly remnant ~2.2 mol Li^+ in the Te lattice caused low Coulombic efficiency near 60%. After the first two cycles, the Coulombic efficiency was greatly improved

(>97%) and the cycle profile thereafter was fairly flat until the 50th cycle. The average charge capacity over the 50 cycles was 609 mA h g^{-1}, corresponding to charge capacity retention of ~99% (Fig. 3d). These results indicate that about 2.9 mol Li^+ per 1.0 mol Te can be reversibly discharged and charged without distinct capacity fading.

As a result, the chemical compositions of the glucose-assisted *co*-carbonized extracellular and intracellular Te materials during cycling can be categorized as follows:

Pristine *c*-Te (*crystalline* extracellular) → $Li_{3.8}Te$ in the 1st discharge ↔ $Li_{1.3}Te$ after the 50th cycle: reversible incorporation of 2.5 mol Li-ion.

Pristine *a*-Te (*amorphous* intracellular) → $Li_{5.2}Te$ in the 1st discharge ↔ $Li_{2.3}Te$ after the 50th cycle: reversible incorporation of 2.9 mol Li-ion.

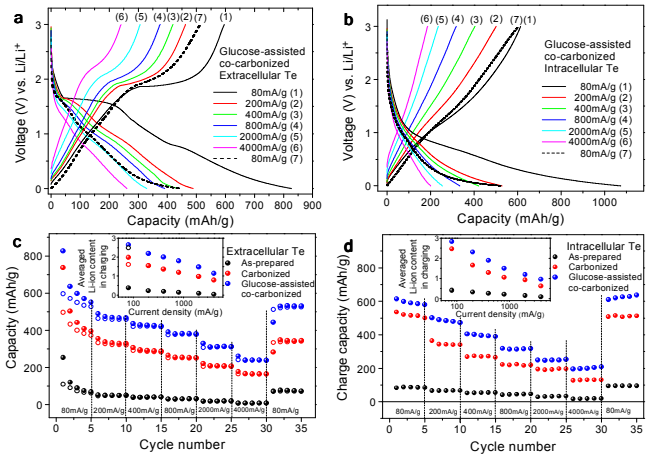

Fig. 4. Rate performance of extracellular and intracellular Te nanorods. The discharge-charge voltage profiles of glucose-assisted *co*-carbonized (**a**) extracellular and (**b**) intracellular Te nanorods with current densities from 80 to 4000 mA g^{-1}. Rate capabilities of glucose-assisted *co*-carbonized (**c**) extracellular and (**d**) intracellular Te over 5 cycles at each current density.

In addition, the rate performances for the extracellular and intracellular Te nanorods were tested under five-step current density profiles from 80 to 4000 mA g^{-1} with identical charging and discharging rates (Fig. 4). In general, a better rate capability is likely to require surface modification for bare nanostructured materials with high surface areas. This is because the solid electrolyte interfaces layer impedes electron and Li-ion transport into/out of the electrode structure, in addition to losses of electrical and mechanical contacts between the nanoparticles. Although the carbonization process can inevitably bring about nanoparticle aggregation and growth, as observed in similar electrochemically active metal-carbon composites, it is possible to maintain more efficient electrical connectivity between the Te domains. As a result, the carbonized Te anodes commonly show meaningful improvements in rate performance at higher rates, compared to the as-prepared Te nanorods. This may be related to the conductive amorphous carbon (~1.1 × 10^2 S m^{-1}) that uniformly covers the surfaces of the Te phases. In both extracellular and intracellular Te nanorods, the charge capacities for the carbonized Te at 2000 mA g^{-1} (25 times faster reaction than 80 mA g^{-1}) were about half of the average capacity at 80 mA g^{-1}. The average charge capacities of the carbonized phase were not too distant from the theoretical capacity of the commercial graphite used in high power density applications. Even more, at 4000 mA g^{-1}, the carbonized Te anodes presented Li-ion uptake abilities close to 1 mol Li-ion.

Li-ion uptake mechanism through *in situ* XAFS and WAXD characterizations

In situ Te K-edge X-ray absorption fine structure (XAFS) analyses for the glucose-assisted *co*-carbonized extracellular and intracellular Te nanorods were performed to obtain real-time structure variations during Li-ion uptake. Such atomic-selective spectroscopic analyses help verify the structural bases that drive the unusual Li-ion storage ability within the Te internal lattice. Figure 5 reveals the effective peak feature variations for both the X-ray absorption near edge structure (XANES) spectra and radial distribution functions (RDF) of the Fourier-transformed (FT) extended X-ray absorption fine structure (EXAFS) spectra for the *co*-carbonized Te anodes during discharging. The Te K-edge XANES spectral features commonly show systematic peak shifts towards the higher energy region during Li-ion uptake. In the conventional XANES concept, this peak behavior indicates the partial oxidation of an X-ray-absorbing central atomic element. Conversely, in the Te K-edge spectra, however, the higher energy peak positions represent the partial reduction of the initially pure metallic Te. This extraordinary spectral feature originates from the electronic configuration of Te(0), which has the [Kr]4d^{10}5s^{2}5p^4 state, and the anion Te^{2-}, which has a fully filled 5p^6 state without any holes. Therefore, the reduced Te in the K-edge absorption experienced an electric-dipole-allowed transition of the 1s electron, not to the fully occupied 5p orbital, but to the next lowest, unoccupied, 6p state. When metallic Te was reduced to anionic Te^{2-}, the K-edge peak position was observed in the higher energy region, as shown for the reference Te materials (Fig. 5a). Thorough analyses of the XANES peak features confirmed the effective reduction of both the extracellular and intracellular metallic Te to the anionic telluride character (Te_n^{2-}) during Li-ion uptake. The higher energy shift during Li-ion uptake was more dominant in the intracellular Te, with ΔE = 4.2 eV, compared to ΔE = 1.3 and 2.0 eV in the bulk and extracellular materials, respectively. This means that the fully lithiated intracellular Te phase possesses a reduced telluride content that exceeds the anionic character of CdTe (ΔE = 2.6), in proportion to the Li-ion uptake amount. Since the element Te intrinsically provided a wide range of polyanions (polytellurides) such as Te^{2-}, Te_2^{2-} and Te_3^{2-} due to the existence of its unusual lone pairs, the Li-ion capacity depends on the tellurium's anionic tolerance in the nanostructured lattice.[40,41]

During Li-ion intercalation into the free spaces between the helical interchains of the Te atomic bundles, therefore, other driving forces for Li-ion uptake can be speculated: the anionic redox chemistry of metallic Te for charge compensation and the Coulombic interactions between electropositive Li^+ and electronegative Te_n^{2-}. However, the Coulombic interaction conducive to Li-ion uptake can also be detrimental to reversible

capacity in the next charging. Since the newly formed Te anion can strongly bind Li^+, the electrostatic interaction between Li^+-Te_n^{2-} ion pairs prevents the reversible release of the intercalated Li-ion in the next charge process, and localized Li_nTe phases remain. Accordingly, the chemical bonds between the inserted Li^+ and anionic Te_n^{2-} cause the formation of a stable Li_nTe phase in each lithiated Te lattice.

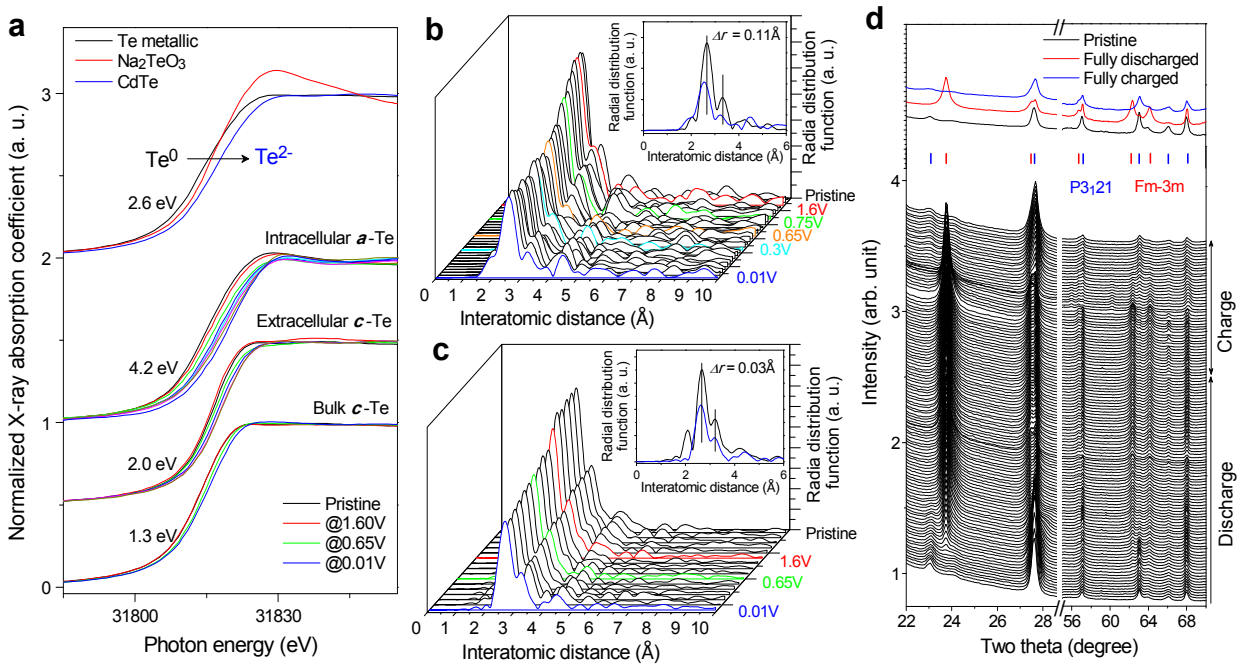

Fig. 5. ***In situ*** **XAFS and WAXD structural characterizations**. (**a**) Normalized Te K-edge XANES spectra of glucose-assisted *co*-carbonized Te during first Li-ion discharging versus reference compounds. (**b**) Radial distribution functions (RDFs) of glucose-assisted *co*-carbonized extracellular Te. (**c**) RDFs of bulk polycrystalline Te. Each inset presents comparative RDFs of the pristine and the fully discharged states. (**d**) *In situ* wide-angle X-ray diffraction patterns of the glucose-assisted *co*-carbonized extracellular Te during the 1st cycle. The calculated Bragg peaks are marked for space groups $P3_121$ (blue) and *Fm-3m* (red) and the XRD patterns are simulated as a function of mole ratio of Te to Li in *Fm-3m* phase (Fig. S11, ESI). Those of the glucose-assisted *co*-carbonized intracellular Te (amorphous phase) are presented in Fig. S12, ESI.

As a result, the initial irreversible capacity drops equivalent to $Li_{1.4}Te$ and $Li_{2.3}Te$ has been observed in both *co*-carbonized extracellular and intracellular materials, respectively. After the initial capacity drop by sacrificial stable Li_nTe phases, the next discharge-charge process could be thereafter reversible.

The RDF features from the *in situ* Te K-edge EXAFS spectra for the polycrystalline glucose-assisted *co*-carbonized Te materials, show the distinct bond characteristics of the first and second FT peaks below 4 Å (Fig. 5b). The first FT peak at 2.8 Å could be assigned to the Te-Te bond distance in the helically zigzagging atomic single intrachain. The second FT peak at 3.4 Å was relevant to the van der Waals radius between Te interchains, corresponding to channels with enough free volume to supply Li-ion intercalation pathways.[34] On discharging, the RDF features present a combination of single plateau and a continuous decrease in the first FT peak intensities, reflecting the voltage profile characteristics. In the *co*-carbonized extracellular material, the constant FT peak features at the first voltage plateau near 1.6 V indicated that the inserted Li-ion can travel freely through the empty spaces between the interchains of Te atomic wires without any structural stress. In the next single smooth voltage region below 1.6 V, the deceasing FT peak patterns reveal that Li^+-Te_n^{2-} chemical bonds newly form around the central Te in the helical chains and linearly increase until fully discharged. After the saturation of Li-ion intercalation between the Te atomic channels, the Te nanorods experienced the gradual formation of Coulombic interactions in proportion to the amount of Li-ion uptake. Accordingly, the ion pairs appear to lead to the partial local distortion of the atomic arrays within the intrachain and atomic channel-to-channel rearrangement in the host Te lattice. Nevertheless, the two typical characteristic FT peaks of the trigonal Te phase were commonly preserved, even with 3.8 mol Li-ion uptake into the *co*-carbonized extracellular nanorods. From the viewpoint of molecular geometry, it is clear that both intrachain and interchain arrays are maintained at the fully discharged state without severe local structural breakage.

In addition, the FT peak positions were obviously shifted towards the lower *r* space region when fully discharged. Such RDF features show that the excess Li-ion uptake beyond the pure intercalation capability promoted volume contractions due to the electrostatic interactions of the Li^+-Te_n^{2-} pairs. According to earlier reports for the similar metallic Sn anode system, the well-known metallic-alloying mechanism through simple Li-ion accumulation to $Li_{4.4}Sn$ leads to a critical expansion of the overall lattice volume, followed by the pulverization of the electrochemically active

electrode particles and severe capacity fading.[42,43] In contrast, the Te exhibited distinct decreases in the Te-Te bond distances during high Li-ion uptake, owing to the conversion of metallic Te to anionic Te_n^{2-} and then the evolution of the Li^+-Te_n^{2-} Coulombic interactions. The volume contraction was more dominant in the extracellular Te material with bond length shrinkage by about 0.11 Å, compared to bulk metallic Te (Fig. 5c). This is because more Li-ion uptake facilitates more Coulombic interactions between the Li^+ and Te_n^{2-} species in the Te atomic-wire bundles.

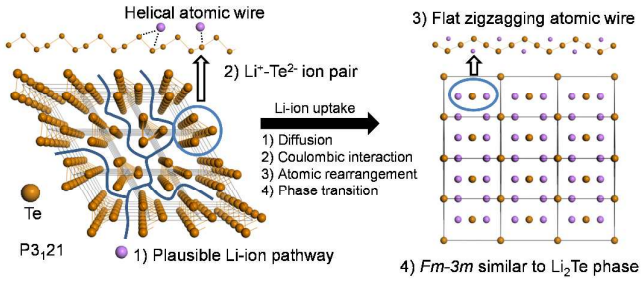

Fig. 6. Internal structure on Li-ion behavior within polycrystalline Te. Geometric basis for Li-ion uptake into the crystallized Te phase through anionic redox chemistry. Li-ion uptake can be induced through the following steps: 1) simple intercalation of Li-ions (purple circles) into empty pathways between the helical atomic wires in the trigonal *P3₁21* phase; 2) reduction of metallic Te (yellow circles) to anionic telluride with formation of Li^+-Te_n^{2-} ion pairs in the lattice; 3) rearrangement of Te atoms in the helical chains to a flattened configuration due to electrostatic interactions; and 4) phase transition to the cubic *Fm-3m* phase.

The effects of the induced electrostatic interactions on the molecular structure of the helical atomic chains and the atomic rearrangement in the wire bundles were investigated by *in situ* wide-angle X-ray diffraction (WAXD) during cycling. *In situ* WAXD patterns for the glucose-assisted *co*-carbonized extracellular Te material show the clear transition from the trigonal $P3_121$ phase to the cubic *Fm*-3*m,* which is very similar to the crystal structure of Li_2Te (Fig. 5d and Fig. S11, ESI). On the other hand, the intracellular Te keeps constant amorphous phase during lithiation-delithiation processes (Fig. S12, ESI). After the first cycle, the Li_2Te phase reverted to the original Te trigonal phase. During Li-ion uptake, the initially helical Te atomic wire was changed to a flat zigzagged atomic ordering in every single chain, due to pressure from the electrostatic interactions of the Li^+-Te^{2-} ion pairs. As a result, the real-time *in situ* XAFS and WAXD results suggest reasonable Li-ion uptake mechanisms for the Te anode materials, as schematically described in Fig. 6. First, the Li-ion is intercalated into the empty channels of the host lattice with zero strain. Then, the increased Li-ion content converts the metallic Te to the anionic Te_n^{2-} through anionic redox chemistry for charge compensation of the excess positive Li^+-ions. The Li^+-Te_n^{2-} ion pairs can be effectively driven into the host lattice of the lithiated Te nanorods. Electrostatic interactions bring about volume shrinkage by way of shorter bond lengths along the intrachains and between the interchains. The ion pairs force the helical atomic wire to be suppressed linear array through a local atomic rearrangement. Then, after the primary sacrifice of the stable irreversible Li_nTe phase, the Li-ion can be reversibly discharged and charged without any irreversible phase changes, as in a Li-ion sponge.

Conclusions

The biological synthetic route for extracellular and intracellular Te nanorods through the bacterial respiration process of *Shewanella oneidensis* MR-1 allows the dual-functionalized potential for both the facile preparation of energy storage nanomaterials and the direct carbonization of electrode materials by bacterial cell burning. Beyond the initial zero-strain Li-ion intercalation into the atomic wire bundle structure of Te element, the carbonized metallic Te nanorods show efficient Li-ion uptake into the atomic wire bundles due to unusual redox chemistry from the flexible electronic characteristics of the element Te. The evolved electrostatic interactions between lithium-telluride ion pairs contribute to the geometric stability against unusually excessive Li-ion positioning in the host Te lattice. With the sacrifice of partial ion-pair remnants, Li-ions can be reversibly taken up and released by way of phase transitions between the metallic and anionic tellurium states without any structural distortion. Especially, the electrostatic interaction between Li^+-Te_n^{2-} ion pairs helped maintain stable lattice volume of host tellurium during Li-ion uptake, highlighting the Te element as a promising Li-rechargeable battery electrode material. Moreover, it is expected that this bacteria-driven biological synthesis can be expanded to the production of other well-defined functional nanomaterials under ambient conditions.

Experimental

Preparation of tellurium nanorods

All chemicals and reagents were purchased from Sigma-Aldrich (St. Louis, MO) and Fisher Scientific (Pittsburgh, PA). Intracellular[5] and extracellular[21] Te nanorods were prepared by the previously reported biological method with minor modifications. *S. oneidensis* MR-1 was grown aerobically on Luria-Bertani (LB) broth at 30°C with shaking at 200 rpm for 12 h. Cells were centrifuged (9000 g for 10 min), washed with sterile 4-(2-hydroxyethyl)-1-piperazineethanesulfonic acid (HEPES) buffer (10 mM, pH 7.0), and resuspended in HEPES buffer. The cells were subsequently inoculated into serum bottles to achieve an optical density (OD) of 0.1 at a wavelength of 600 nm of the total volume of sterilized HEPES-buffered basal medium. Ten mM sodium lactate (0.22 µm filter-sterilized) was used as the electron donor for both intracellular and extracellular Te nanorods. For the synthesis of intracellular Te nanorods, 100 µM sodium tellurite (Na_2TeO_3) was used as the final electron acceptor, while for the synthesis of extracellular Te nanorods, 1 mM Na_2TeO_3 and 10 mM Fe(III)-citrate were used as the electron acceptors. All incubations were carried out in the absence of light without agitation at 30 °C under anaerobic conditions. The intracellular and extracellular Te nanorods were centrifuged (9000g for 10 min) and washed with deionized water after 5 d and 1 d incubation, respectively. Samples were dried under anoxic conditions.

Carbonization of tellurium nanorods

Primary carbonized Te nanorods were prepared through thermal treatment. Intracellular and extracellular Te nanorods were directly heat-treated in an alumina tube at 600 °C for 3 h under N_2 flow of 0.15 L min^{-1}. For the glucose-driven *co*-carbonized Te nanorods, different amounts of D-(+)-glucose were dissolved in deionized water, and the biologically generated Te nanorods were added to obtain suspensions with weight ratios of Te nanorods to glucose of 2:1, 4:1, and 10:1. The suspensions were freeze-dried under anoxic conditions. To remove the bacterial cells from the Te nanorods, the as-prepared extracellular and intracellular materials were heated in an alumina tube at 300 and 600 °C for 3 and 6 h under N_2 flow of 0.15 L min^{-1}. After heating, the samples were slowly cooled or quenched to room temperature. All samples were maintained in an inert atmosphere until use.

Characterization and analysis

Suspensions of all tellurium samples were dropped and dried on silica wafers for the scanning electron microscopy (SEM) analyses, which were operated at 10 kV (SEM, XL30-FEG, Philips, Eindhoven, Netherlands). For transmission electron microscopy (TEM) analysis, suspensions were placed onto carbon-coated 200-mesh copper grids. The images of whole mounts were obtained at 200 kV using a JEOL TEM-2100 high resolution TEM (JEOL, Tokyo, Japan). The geometric structure of the Te nanorods was analyzed using powder X-ray diffraction (XRD, D/MAX Uitima III, Rigaku, Tokyo, Japan) equipped with monochromatic high-intensity Cu Kα radiation (λ = 1.54056 Å). Thermogravimetric analysis (TGA) were performed in N_2 flow on heating to 700 °C at a rate of 10 °C/min using a TG/DTA-6300 of Seiko thermogravimeter. Differential scanning calorimetric (DSC) analysis were performed in N_2 flow on heating to 450 °C at a rate of 10 °C/min and on cooling to 40 °C at a rate of 20 °C/min using a DSC Q20 of TA Instruments.

Electrochemistry

The Te electrodes were composed of the extracellular or intracellular Te nanorods, Ketjen Black, and polyvinylidene difluoride (PVdF) binder in a weight ratio of 70:15:15 on pure Cu foil. Coin-type half cells (2032-type) were assembled in an Ar-filled glove box, using lithium metal foil as the counter electrode, microporous polyethylene as the separator, and 1.15 M $LiPF_6$ in ethylene carbonate/diethylene carbonate/ethyl-methyl carbonate (EC/DEC/EMC, 3:2:5 v/v) as an electrolyte. The loading amount of the electrode material was measured as >1 mg cm^{-2}. The cell tests were performed with a WBCS3000 automatic battery cycler system (Wonatech Co.), and the capacity was estimated based only on active material. Discharge-charge voltage profiles of as-prepared, primary carbonized, and glucose-*co*-carbonized extracellular and intracellular Te nanomaterials were tested with current densities from 80 to 4000 mA g^{-1} and cutoff voltage window of 0.01-3.0 V using coin-type lithium half-cells.

***In situ* XAFS and WAXD characterization**

In situ Te K-edge X-ray absorption spectra of the extracellular and intracellular Te nanorods, X-ray absorption near edge structure (XANES), and extended X-ray absorption fine structure (EXAFS), were collected on the BL10C beam line (WEXAFS) at the Pohang light source (PLS-II) with top-up mode operation under a ring current of 300 mA at 3.0 GeV. From the high intensity X-ray photons of the multipole wiggler source, monochromatic X-ray beams could be obtained using a liquid-nitrogen-cooled double-crystal monochromator (Bruker ASC) with available *in situ* exchange in vacuum between a Si(111) and Si(311) crystal pair. The Si(311) crystal pair was used for Te K-edge XAFS measurements (absorption edge energy, 31814 eV) for better energy resolution. Real-time Te K-edge X-ray absorption spectroscopic data during discharging and charging processes were recorded for a Te electrode assembled in a home-made *in situ* electrochemical cell with polyimide film windows (Swagelok-type cell, Fig. S13, ESI), in transmittance/fluorescence modes using passivated implanted planar silicon (PIPS, Canberra Co.) as a fluorescence detector and Ar/N_2 gas-filled ionization chambers (IC-SPEC, FMB Oxford) for the incident and transmitted X-ray photons. Higher-order harmonic contaminations were eliminated by detuning to reduce the incident X-ray intensity by ~30%. Energy calibration was simultaneously carried out for each measurement with reference Te bulk metallic powder placed in front of the third ion chamber. The data reductions of the experimental spectra to normalized XANES and Fourier-transformed radial distribution functions (RDFs) were performed through the standard XAFS procedure.

Another *in-situ* structural characterization was carried out at the BL9A beamline (U-SAXS) for the wide-angle X-ray diffraction (WAXD) measurements. The X-rays coming from the *in-vacuum* undulator (IVU) were monochromated (wavelength, λ = 0.6213 Å) using a Si(111) double-crystal monochromator and focused using a K-B type mirror system to be ca. 350 μm (H) × 30 μm (V) (full-width-at-half-maximum) at the sample position. The *in situ* WAXD test cell was made by modifying a commercial coin cell (CR2032) in which a 3-mm (dia.) through-hole was drilled at the center region for X-ray transmission, and the entrance and exit openings were glued over with 15 μm-thick polyimide films to hold the inner battery components. The test cells were positioned on a motorized multi-cell stage and, during the charging and discharging cycles, *in situ* WAXD patterns were recorded about every 5 minutes with a 2D CCD detector (SX165, Rayonix LLC, USA). The X-ray exposure time was 10 s for each shot. For clarity, the diffraction angles were finally converted to those of Cu K□radiation (λ = 1.5418 Å) after a calibration process with NIST standard LaB_6 (SRM 660b). Because the main Bragg peaks for the Cu foil as current collector in the *in situ* cell assembly are observed in the Bragg angle region between 30 and 55°, a circular lead was used to block the corresponding 2θ region in front of the CCD detector. The 2θ shielding afforded enhanced XRD patterns for the thin Te electrodes.

Acknowledgements

This research was supported by the Basic Science Research Program through the National Research Foundation of Korea (NRF) funded by the Ministry of Education, Science and Technology (2010-0029224 and 2012R1A1A2043811). Synchrotron-based experiments performed at Pohang Light Source II (PLS-II) were supported in part by the Ministry of Education and POSTECH. All authors thank W. W.

Lee and S. W. Kang (PAL) for the assistance of in situ experimental measurements

Notes and references

1. A. Klonowska, T. Heulin and A. Vermeglio, *Appl. Environ. Microbiol.,* 2005, **71**, 5607-5609.
2. J. K. Fredrickson, M. F. Romine, A. S. Beliaev, J. M. Auchtung, M. E. Driscoll, T. S. Gardner, K. H. Nealson, A. L. Osterman, G. Pinchuk and J. L. Reed, *Nat. Rev. Microbiol.,* 2008, **6**, 592-603.
3. D. Zannoni, F. Borsetti, J. J. Harrison and R. J. Turner, *Adv. Microb. Physiol.,* 2008, **53**, 1-72.
4. J. R. Lloyd, J. M. Byrne and V. S. Coker, *Curr. Opin. Biotechnol.,* 2011, **22**, 509-515.
5. D. H. Kim, R. A. Kanaly and H. G. Hur, *Bioresour. Technol.,* 2012, **125**, 127-131.
6. J. H. Lee, M. G. Kim, B. Yoo, N. V. Myung, J. Maeng, T. Lee, A. C. Dohnalkova, J. K. Fredrickson, M. J. Sadowsky and H.-G. Hur, *Proc. Natl. Acad. Sci. U. S.A.,* 2007, **104**, 20410-20415.
7. S. Jiang, F. Liu, M. G. Kim, J.-H. Lim, K.-J. Lee, Y.-H. Choa, K. Song, M. J. Sadowsky, W. Chen and N. V. Myung, *J. Mater. Chem.,* 2011, **21**, 10277-10279.
8. L. Manna, D. J. Milliron, A. Meisel, E. C. Scher and A. P. Alivisatos, *Nat. Mater.*, 2003, **2**, 382-385.
9. S. Srivastava, A. Santos, K. Critchley, K. S. Kim, P. Podsiadlo, K. Sun, J. Lee, C. Xu, G. D. Lilly, S. C. Glotzer and N. A. Kotov, *Science*, 2010, **327**, 1355-1359.
10. K. Zweibel, *Science*, 2010, **328**, 699-701.
11. T. I. Lee, S. Lee, E. Lee, S. Sohn, Y. Lee, G. Moon, D. Kim, Y. S. Kim, J. M. Myoung and Z. L. Wang, *Adv. Mater.*, 2013, **25**, 2920-2925.
12. G. Zhang, W. Wang and X. Li, *Adv. Mater.*, 2008, **20**, 3654-3656.
13. G. Zhang, B. Kirk, L. A. Jauregui, H. Yang, X. Xu, Y. P. Chen and Y. Wu, *Nano Lett.*, 2012, **12**, 56-60.
14. D. Lencer, M. Salinga, B. Grabowski, T. Hickel, J. Neugebauer and M. Wuttig, *Nat. Mater.*, 2008, **7**, 972-977.
15. T. Siegrist, P. Jost, H. Volker, M. Woda, P. Merkelbach, C. Schlockermann and M. Wuttig, *Nat. Mater.*, 2011, **10**, 202-208.
16. G. Atwood, *Science*, 2008, **321**, 210-211.
17. R. J. Turner, R. Borghese and D. Zannoni, *Biotechnol. Adv.*, 2012, **30**, 954-963.
18. T. G. Chasteen, D. E. Fuentes, J. C. Tantalean and C. C. Vasquez, *FEMS Microbiol. Rev.*, 2009, **33**, 820-832.
19. S. M. Baesman, T. D. Bullen, J. Dewald, D. Zhang, S. Curran, F. S. Islam, T. J. Beveridge and R. S. Oremland, *Appl. Environ. Microbiol.*, 2007, **73**, 2135-2143.
20. L. A. Ba, M. Doring, V. Jamier and C. Jacob, *Org. Biomol. Chem.*, 2010, **8**, 4203-4216.
21. D. H. Kim, M. G. Kim, S. Jiang, J. H. Lee and H. G. Hur, *Environ. Sci. Technol.,* 2013, **47**, 8709-8715.
22. Z. Liu, Z. Hu, J. Liang, S. Li, Y. Yang, S. Peng and Y. Qian, *Langmuir*, 2004, **20**, 214-218.
23. Y. J. Zhu, W. W. Wang, R. J. Qi and X. L. Hu, *Angew. Chem., Int. Ed.*, 2004, **43**, 1410-1414.
24. H. S. Qian, S. H. Yu, J. Y. Gong, L. B. Luo and L. f. Fei, *Langmuir*, 2006, **22**, 3830-3835.
25. Q. Wang, G. D. Li, Y. L. Liu, S. Xu, K. J. Wang and J. S. Chen, *J. Phys. Chem.*, 2007, **111**, 12926-12932.
26. D. H. Webber and R. L. Brutchey, *Chem. Commun.*, 2009, 5701-5703.
27. T. Vasileiadis, V. Dracopoulos, M. Kollia and S. N. Yannopoulos, *Sci. Rep.*, 2013, **3**, 1209.
28. H. Zhu, H. Zhang, J. Liang, G. Rao, J. Li, G. Liu, Z. Du, H. Fan and J. Luo, *J. Phys. Chem.*, 2011, **115**, 6375-6380.
29. Z. Tang, Y. Wang, K. Sun and N. A. Kotov, *Adv. Mater.*, 2005, **17**, 358-363.
30. J. M. Shen, J. Y. Li, Y. Chen and Z. Huang, *J. Phys. Chem.*, 2009, **113**, 9502-9508.
31. J. W. Liu, W. R. Huang, M. Gong, M. Zhang, J. L. Wang, J. Zheng and S. H. Yu, *Adv. Mater.*, 2013, **25**, 5910-5915.
32. L. Yang, Z. G. Chen, G. Han, L. Cheng, H. Xu and J. Zou, *Cryst. Growth Des.*, 2013, **13**, 4796-4802.
33. X. Wu, Y. Wang, S. Zhou, X. Y. Yuan, T. Gao, K. Wang, S. Lou, Y. Liu and X. Shi, *Cryst. Growth Des.*, 2012, **13**, 136-142.
34. H. Ikemoto, A. Goyo and T. Miyanaga, *J. Phys. Chem.*, 2011, **115**, 2931-2937.
35. Y. Liu, J. Wang, Y. Xu, Y. Zhu, D. Bigio and C. Wang, *J. Mater. Chem. A*, 2014, **2**, 12201-12207.
36. N. Ding, S. F. Chen, D. S. Geng, S. W. Chien, T. An, T. S. A. Hor, Z. L. Liu, S. H. Yu and Y. Zong, *Adv. Energy Mater.*, 2015, **5**, 1401999.
37. K. T. Nam, D. W. Kim, P. J. Yoo, C. Y. Chiang, N. Meethong, P. T. Hammond, Y. M. Chiang and A. M. Belcher, *Science*, 2006, **312**, 885-888.
38. X. Chen, K. Gerasopoulos, J. Guo, A. Brown, C. Wang, R. Ghodssi and J. N. Culver, *ACS Nano*, 2010, **4**, 5366-5372.
39. M. Noh, Y. Kwon, H. Lee, J. Cho, Y. Kim and M. G. Kim, *Chem. Mater.*, 2005, **17**, 1926-1929.
40. S. Deng, A. Köhler and A. Simon, *Angew. Chem., Int. Ed.*, 2006, **45**, 599-602.
41. T. Chivers, *J. Chem. Soc., Dalton Trans.*, 1996, 1185-1194.
42. W. M. Zhang, J. S. Hu, Y. G. Guo, S. F. Zheng, L. S. Zhong, W. G. Song and L. J. Wan, *Adv. Mater.*, 2008, **20**, 1160-1165.
43. D. Deng, M. G. Kim, J. Y. Lee and J. Cho, *Energy Environ. Sci.*, 2009, **2**, 818-837.

A table of contents entry

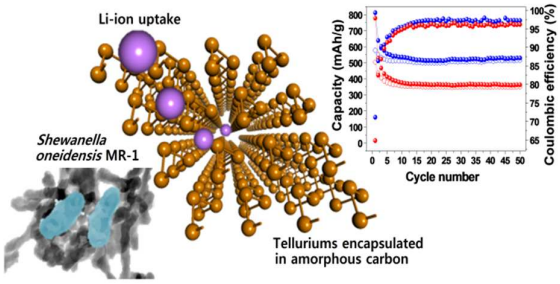

Li-ion storage through anionic redox process of biogenic Tellurium nanorods to provide biogeochemistry with new insight into energy science and vice versa.